2024 IEEE/RSJ International Conference on Intelligent Robots and Systems (IROS)
October 14-18, 2024. Abu Dhabi, UAE

Design of a Variable Wheel-propeller Integrated Mechanism for Amphibious Robots

Liang Lu[1,2*], Xiangquan Gao[2*], Ming Xiang[2], Zefeng Yan[2] and Bin Han[2†], *Member, IEEE*

***Abstract*— In order to address the high complexity and low efficiency of amphibious propulsion systems, this paper proposes a novel variable wheel-propeller integrated mechanism for amphibious robots. By adjusting the blade pitch angle, it enables multiple motion modes, including rapid and stable movement on flat ground, obstacle crossing, and omnidirectional movement on water surface. This study establishes a kinematic model for the propeller blades and conducts multi-objective optimization of the structural parameters by considering both the land obstacle-crossing performance and underwater propulsion performance. Based on the optimized structural parameters, a virtual simulation prototype is constructed. Simulation results indicate that when water surface movement, with a driving torque of 3N.m, robot achieves a maximum linear velocity of 1.25m/s and a maximum angular self-rotation velocity of 3.5rad/s. Moreover, varying the blade pitch angle can alter the thrust direction, enabling omnidirectional mobility on water surface. During land movement, with a rotation speed of 60rpm, the highest obstacle-crossing height is 184mm. This wheel-propeller integrated mechanism exhibits robust comprehensive motion performance and environmental adaptability, with convenient motion modes switching.**

I. INTRODUCTION

Amphibious robots combine the characteristics of land and underwater robots, enabling them to perform tasks in complex aquatic and terrestrial environments, including jungles, marshlands, and coastal areas [1][2]. Owing to their notable advantages, amphibious robots find wide-ranging applications in research, urban infrastructure inspection, military domains. Therefore, the development of amphibious propulsion mechanisms with high mobility and high environmental adaptability is of paramount importance.

To achieve amphibious capabilities, many robots have been designed with two distinct propulsion systems [1]. Examples include the AmphiRobot-II [3], the Salamandra robotica II [4], the bionic crab robot [5], and so on. Various schemes combine terrestrial propulsion systems such as legs, wheels, tracks, with aquatic propulsion systems such as propellers, fins, and flippers [6]. These combined propulsion schemes primarily enable amphibious capabilities, but such schemes require time for propulsion system switching, which reduces their efficiency and reliability [1].

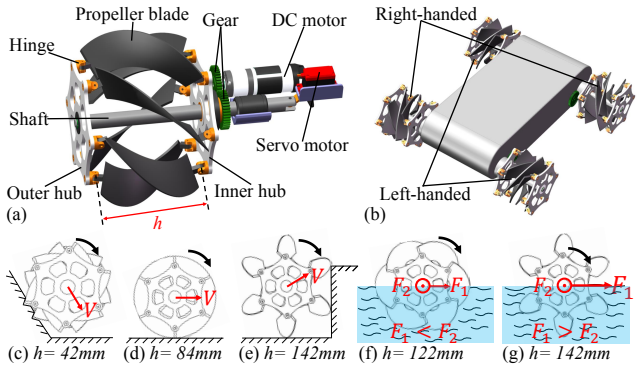

Fig. 1. Schematic sketch of a wheel-propeller integrated mechanism module. (a) Wheel-propeller integrated mechanism module, (b) Wheel-propeller integrated mechanism based amphibious robot, (c) Driving on soft terrain, (d) Driving on flat terrain, (e) Obstacle crossing, (f) Water surface lateral propulsion, (g) Water surface forward propulsion.

Thus, some researchers have turned their attention to composite propulsion mechanisms, developing a series of leg-flipper, biomimetic, and wheel-propeller mechanisms. Amphibious robots with leg-flippers [6][7], bionic snakes [8][9], bionic turtle [10], and undulatory fins [11][12] propulsion mechanisms have mitigated the traditional drawback of "one system working while the other is idle". However, they still lack the amphibious traversal capabilities for high-speed and multi-modal when faced with unstructured environments and complex coupled tasks. Wheel-propeller propulsion mechanisms, which combine the advantages of wheels for terrestrial movement and propellers for aquatic use, offer higher speed, efficiency, and ease of transition between water and land. Sun et al. proposed an eccentric paddle mechanism that combines wheels and paddles [13]. Pu et al. proposed a novel non-reciprocal leg gait [14], and Shen et al. designed a forward crawling underwater propulsion mode, both aimed at improving the eccentric paddle mechanism [15]. Claveria et al., with reference to the LDR-2 wheeled-leg mobile robot developed by Bai's team [16], designed a multi-terrain vehicle named ROGV that seamlessly integrates various capabilities including climbing, rolling, and water-crossing [17]. Huang et al. introduced a wheel-paddle composite amphibious robot that achieves the motion transformation from land to water by the thermal stimulation deformation response [18]. Wu et al. [19] and Yu et al. [20] separately designed composite propulsion robots that combine propellers with tracks or leg mechanisms. Current wheel-propeller composite propulsion mechanism

This work was supported in part by the National Natural Science Foundation of China (52375015), in part by the Interdiciplinary Research Program(Robotics and Artificial Intelligence) of HUST ThunderGrant (2024JCYJ037) and in part by the Natural Science Foundation Hubei Province of China (2022CFB239).

[1] School of Artificial Intelligence and Automation, Huazhong University of Science and Technology, Wuhan 430074, china. [2] State Key Laboratory of Intelligent Manufacturing Equipment and Technology, School of Mechanical Science and Engineering, Huazhong University of Science and Technology, Wuhan 430074, china.

[*] These authors contributed equally to this work.

[†] Corresponding auther, binhan@hust.edu.cn

has a complex structure, low aquatic propulsion efficiency, and especially cannot achieve omnidirectional mobility.

The study introduces a novel variable wheel-propeller integrated mechanism for amphibious robots, as illustrated in Fig.1. By adjusting the distance between the inner and outer hubs, the blade pitch angle can be changed, thereby altering the morphology of the mechanism to adapt to different terrains, such as soft terrain, flat terrain, obstacle crossing, and even omnidirectional mobility on water surface. This mechanism ensures high performance movement in various modes while maintaining low structural complexity, thus offering significant advantages in maneuverability, efficiency, and reliability.

II. KINEMATIC MODELING OF BLADES

The propeller blades are hinged at both ends to the inner and outer hubs, as shown in Fig.1. By adjusting the distance between the inner and outer hubs, the blade pitch angle can be varied, thereby imparting various motion capabilities.

During the adjustment of the distance between the inner and outer hubs, a model for the pose changes of the blades is developed, with the model typically neglecting the blade thickness. Firstly, the shape of the blade is described by the helical surface equation, and then the pose of the blade is mapped to the shaft coordinate system by the homogeneous transformation matrix. As depicted in Fig. 2, a blade surface coordinate system $o_2 - x_2y_2z_2$ is established, where the z_2 axis is along the height of the spiral and the y_2 axis is along the inner side of the spiral. In the blade surface coordinate system $o_2 - x_2y_2z_2$, the position of point p on the blade surface is expressed as:

$$^{2}\boldsymbol{p} = \left[{}^{2}p_x, {}^{2}p_y, {}^{2}p_z\right]^T \tag{1}$$

$$\begin{cases} p_x = D \times r \times \sin(\dfrac{\theta}{2} \times \dfrac{z}{h/2}) \\ p_y = -r \times \cos(\dfrac{\theta}{2} \times \dfrac{z}{h/2}) \\ p_y = z \end{cases} \tag{2}$$

$$r \in [d/2 - w_1, d/2 + w_2] \tag{3}$$

$$z \in [-h/2, h/2] \tag{4}$$

Where, D denotes the spiral direction of the blade, with $D = 1$ indicating right-handed blade and $D = -1$ indicating left-handed blade. The variables r and z are used to describe the spatial coordinates of point p on the blade surface. Meanwhile, d, h, θ respectively represent the diameter, height, and total helical angle of the blade helix. Additionally, w_1 is the inward blade width at the hinge, and w_2 is the outward blade width at the hinge.

As depicted in Fig.3, the shaft coordinate system $o_1 - x_1y_1z_1$ is established. At the initial position, the x_1 axis is along the robot's forward direction, the y_1 axis is along the longitudinal direction, and the z_1 axis is along the axis of shaft. $o_0 - x_0y_0z_0$ is base coordinate system. Disregard the thickness at the hinge, when the distance between the inner and outer hubs changes from h to h', the coordinate system

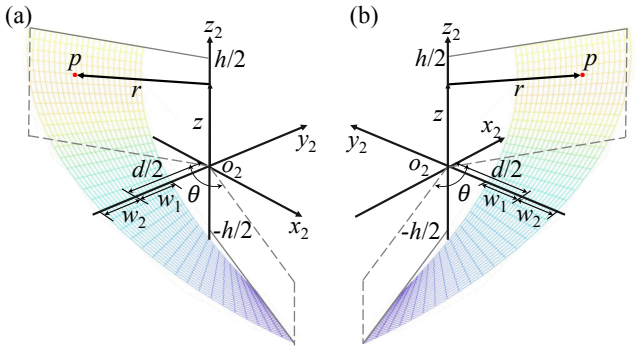

Fig. 2. The coordinate system of blade surface. (a) Left-handed blade, (b) Right-handed blade.

$o_2 - x_2y_2z_2$ has an offset distance b along the y_1 axis and a deflection angle β around the y_1 axis at the same time.

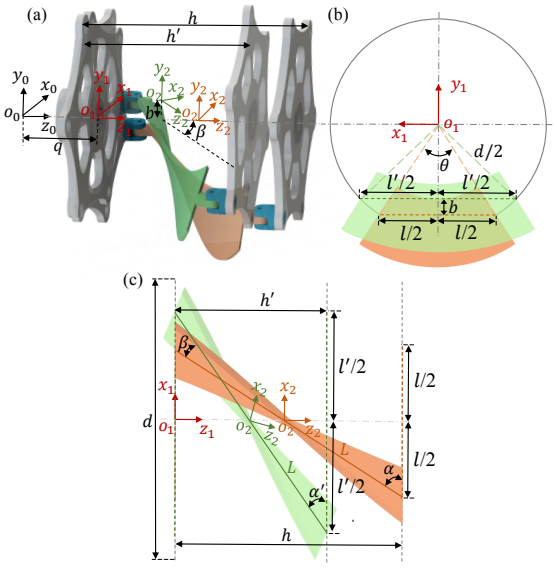

Fig. 3. The pose transformation of the coordinate system $o_2 - x_2y_2z_2$ relative to the coordinate system $o_1 - x_1y_1z_1$. (a) The coordinate system $o_1 - x_1y_1z_1$ of shaft, (b) The projection of the blade in $x_1o_1y_1$ plane, (c) The projection of the blade in $x_1o_1z_1$ plane.

When the distance between the inner and outer hubs is h, the projected length l of the blade's two end hinges within the $x_1o_1y_1$ plane is given by:

$$l = d \times \sin(\theta/2) \tag{5}$$

At this time, the length of the line connecting the two end hinges of the blade is:

$$L = \sqrt{h^2 + l^2} \tag{6}$$

When the distance between the inner and outer hub changes to h', the deflection angle β of the coordinate system $o_2 - x_2y_2z_2$ around the y_1 axis is:

$$\beta = D \times (\alpha - \alpha') \tag{7}$$

$$\alpha = \arctan(h/l) \tag{8}$$

$$\alpha' = \arcsin(h'/L) \tag{9}$$

At this time, the projected length l' of the blade's two end hinges in the $x_1o_1y_1$ plane is given by:

$$l' = h'/\tan\alpha' \tag{10}$$

It can be obtained that the offset distance b of the coordinate system $o_2 - x_2y_2z_2$ along the y_1 axis is:

$$b = \sqrt{(d/2)^2 - (l/2)^2} - \sqrt{(d/2)^2 - (l'/2)^2} \tag{11}$$

Thus, the spatial position of point p on the blade surface in the coordinate system $o_1 - x_1y_1z_1$ is denoted as:

$$^{1}\boldsymbol{p} = \left[{}^{1}p_x, {}^{1}p_y, {}^{1}p_z\right]^T \tag{12}$$

$$\begin{bmatrix} {}^{1}\boldsymbol{p} \\ 1 \end{bmatrix} = \begin{bmatrix} \cos\beta & 0 & \sin\beta & 0 \\ 0 & 1 & 0 & b \\ -\sin\beta & 0 & \cos\beta & h'/2 \\ 0 & 0 & 0 & 1 \end{bmatrix} \begin{bmatrix} {}^{2}\boldsymbol{p} \\ 1 \end{bmatrix} \tag{13}$$

If the wheel-propeller integrated mechanism rotates at an angular speed ω around the rotation shaft for time t and the rotation angle of the shaft coordinate system $o_1 - x_1y_1z_1$ around z_0 is $\varphi = \omega t$. Then the spatial position of the point p in the coordinate system $o_0 - x_0y_0z_0$ is:

$$^{0}\boldsymbol{p} = \left[{}^{0}p_x, {}^{0}p_y, {}^{0}p_z\right]^T \tag{14}$$

$$\begin{bmatrix} {}^{0}\boldsymbol{p} \\ 1 \end{bmatrix} = \begin{bmatrix} \cos\varphi & -\sin\varphi & 0 & 0 \\ \sin\varphi & \cos\varphi & 0 & 0 \\ 0 & 0 & 1 & q \\ 0 & 0 & 0 & 1 \end{bmatrix} \begin{bmatrix} {}^{1}\boldsymbol{p} \\ 1 \end{bmatrix} \tag{15}$$

III. DESIGN OF STRUCTURAL PARAMETERS

After kinematic modeling of blades, it is necessary to analyze the influence of these structural parameters on the water surface and land motion performances and finally give the ideal structural parameters.

A. Analysis of Underwater Propulsion Performance

To obtain the underwater thrust characteristics of the wheel-propeller integrated mechanism, an additional underwater propulsion model for a single blade is developed based on the aforementioned blade motion equations and hydrodynamics theory [21]. According to the fluid drag theory, fluid force can be regarded as the vector sum of the normal force $\boldsymbol{f_n}$ and the tangential force $\boldsymbol{f_\tau}$:

$$\boldsymbol{f_n} = \frac{1}{2}\rho C_S \|\boldsymbol{v_n}\|^2 \boldsymbol{v_{e_{np}}} \tag{16}$$

$$\boldsymbol{f_\tau} = \frac{1}{2}\rho C_S \|\boldsymbol{v_\tau}\|^2 \boldsymbol{v_{e_{\tau p}}} \tag{17}$$

The kinetics analysis problem of the wheel-propeller integrated mechanism in this paper belongs to the high Reynolds number (Reynolds number $\geq 5 \times 10^5$) fluid dynamics problem. The viscous force is much smaller than the pressure, so the effects of viscous force are not considered [22]. A micro-element surface can be intercepted on the blade surface, and the stress distribution on the micro-element surface can be obtained according to the fluid drag theory. Finally, the curved surface is integrated along the blade surface to obtain each component force. The analysis diagram is shown in Fig.4 (a), the expression for the velocity $\boldsymbol{v_p}$ of a micro-element surface is given by:

$$\boldsymbol{v_p} = \frac{\partial^0 \boldsymbol{p}}{\partial t} = \left[\frac{\partial^0 p_x}{\partial t}, \frac{\partial^0 p_y}{\partial t}, \frac{\partial^0 p_z}{\partial t}\right]^T \tag{18}$$

The normal vector of the micro-element is:

$$\boldsymbol{n_p} = \frac{\partial^0 \boldsymbol{p}}{\partial z} \times \frac{\partial^0 \boldsymbol{p}}{\partial r} \tag{19}$$

The unit normal vector of the micro-element is:

$$\boldsymbol{e_{np}} = \frac{\boldsymbol{n}_p}{\|\boldsymbol{n_p}\|} \tag{20}$$

The unit normal vector of the micro-element velocity is:

$$\boldsymbol{v_{e_{np}}} = \frac{\boldsymbol{v_n}}{\|\boldsymbol{v_n}\|} = \frac{(\boldsymbol{v_p} \cdot \boldsymbol{e_{np}}) \cdot \boldsymbol{e_{np}}}{\|(\boldsymbol{v_p} \cdot \boldsymbol{e_{np}}) \cdot \boldsymbol{e_{np}}\|} \tag{21}$$

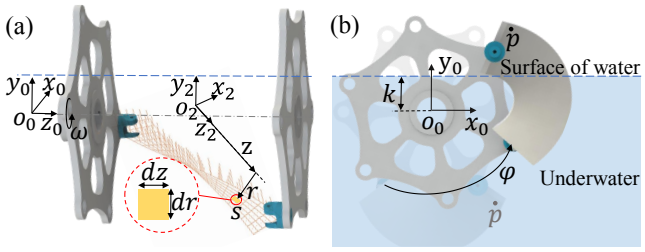

Fig. 4. Hydrodynamics analysis of underwater propulsion. (a) Micro-elemental analysis of blade surface, (b) The process of exiting the water.

When the wheel-propeller integrated mechanism is not fully submerged in water, the blades experience a process of entering and exiting the water, as is shown in Fig. 4 (b). During this process, the proportion of the blade immersed in water will change, leading to variations in the generated thrust. Therefore, when performing the above calculation for micro-element surface, it is necessary to determine whether the micro-element surface is the submerged effective part at that moment. When the distance of the water surface from the shaft is k, the following equation can be obtained:

$$\boldsymbol{f_n} = \begin{cases} \frac{1}{2}\rho C_S \|\boldsymbol{v_n}\|^2 \boldsymbol{v_{e_{np}}}, {}^0p_y \leq k \\ [0,0,0]^T, {}^0p_y > k \end{cases} \tag{22}$$

When the whole blade is rotated to the angle φ, the reaction force of water is:

$$\begin{aligned} \boldsymbol{F} &= -\iint_D \boldsymbol{f_n} dS \\ &= -\int_{-\frac{h}{2}}^{\frac{h}{2}} \int_{-\frac{d}{2}-w_1}^{\frac{d}{2}+w_2} \boldsymbol{f_n} \sqrt{UV - W^2} dr dz \end{aligned} \tag{23}$$

$$\begin{cases} U = \left(\dfrac{\partial^0 p_x}{\partial r}\right)^2 + \left(\dfrac{\partial^0 p_y}{\partial r}\right)^2 + \left(\dfrac{\partial^0 p_z}{\partial r}\right)^2 \\ V = \left(\dfrac{\partial^0 p_x}{\partial z}\right)^2 + \left(\dfrac{\partial^0 p_y}{\partial z}\right)^2 + \left(\dfrac{\partial^0 p_z}{\partial z}\right)^2 \\ W = \dfrac{\partial^0 p_x}{\partial r}\dfrac{\partial^0 p_x}{\partial z} + \dfrac{\partial^0 p_y}{\partial r}\dfrac{\partial^0 p_y}{\partial z} + \dfrac{\partial^0 p_z}{\partial r}\dfrac{\partial^0 p_z}{\partial z} \end{cases} \tag{24}$$

If a single wheel-propeller integrated mechanism is composed of N blades, the total force acting on the wheel-propeller integrated mechanism, $\boldsymbol{F_{all}}$, is formed by the hydrodynamic forces acting on each blades, and there is a phase relationship between the hydrodynamic forces acting on each blade.

$$\boldsymbol{F_i} = \boldsymbol{F}(\boldsymbol{\varphi_i}) \tag{25}$$

$$\boldsymbol{F_{all}} = [F_{x\_all}, F_{y\_all}, F_{z\_all}]^T = \sum_{i=1}^{N} \boldsymbol{F_i} \tag{26}$$

Where, φ is the rotation angle of the first blade, i represents the ith blade, $\varphi_i = \varphi + (i-1) \times 2\pi/N$, and $\boldsymbol{F_i}$ is the force of water on the ith blade.

B. Analysis of Land Obstacle-crossing Performance

When the maximum distance between the inner and outer hubs is L, the entire blade is elongated along the axis direction, resulting in the wheel having its maximum obstacle-crossing capability. As shown in Fig.5, the influence of varying blade quantities on the wheel's maximum obstacle crossing height is analyzed respectively. It can be inferred that the maximum obstacle-crossing height of the wheel $(H_1 + H_2)$ is approximated as a function of the length C and the angle $\Delta\varphi$:

$$\Delta\varphi = 2\pi/N \tag{27}$$

$$C = d/2 + w_2 + d/2(1 - cos(\theta/2)) \tag{28}$$

$$H_1 = C \times \sin(\Delta\varphi/2) \tag{29}$$

$$H_2 = \begin{cases} C \times \cos(\Delta\varphi \times (\dfrac{N-2}{2}) - \dfrac{\pi}{2}), N = 2m+1 \\ C \times \sin(\Delta\varphi \times (\dfrac{N}{4})), N = 2m \end{cases} \tag{30}$$

Where m is a positive integer and the precondition to be satisfied by the above formula is:

$$C \times \cos(\Delta\varphi/2) \geq \frac{d}{2} \tag{31}$$

C. Optimization Design

The two design indexes, namely the forward thrust generated by one revolution of the wheel-propeller integrated mechanism underwater and the maximum obstacle crossing height on land, are selected as the optimization objectives. To achieve this optimization, a multi-objective optimization algorithm, NSGA-II, is applied to optimize the multi-objective functions. Finally, the optimized parameters for the wheel-propeller integrated mechanism are obtained. The details of the optimization formulation are presented in what follows.

Design variables: h, θ, w_1, w_2 and N

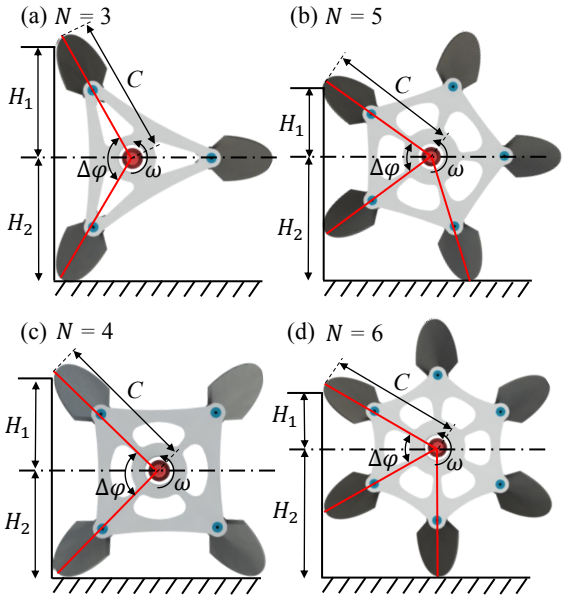

Fig. 5. Obstacle-crossing analysis with different blade quantities.

Constant values:

$$d = 150mm$$
$$\omega = 60rpm$$
$$k = 0mm$$

Constraints:

$$g_1 : \theta \geq \frac{2\pi}{N}$$
$$g_2 : 2 \leq N \leq 10$$
$$g_3 : C \times \cos(\frac{\Delta\varphi}{2}) \geq \frac{d}{2}$$
$$g_4 : L < d$$
$$g_5 : w_1 = w_2$$
$$g_6 : w_1 + w_2 \leq \tfrac{d}{3}$$

Objective function:

$$maximize : -\int_0^{2\pi} F_{x\_all} d\varphi$$
$$maximize : H_1 + H_2$$

Among these constraints, g_1 ensures that the overlap ratio of the blade's outer contour arc in the circular form is greater than 1 for flat terrestrial movement. g_2 restricts the number of blades within a reasonable range. g_3 is a prerequisite for obstacle-crossing capability. g_4 ensures sufficient compressible spacing between the inner and outer hubs. g_5 promotes symmetry in blade shape. g_6 represents the ratio of hub diameter d to the sum of blade widths $(w_1 + w_2)$, while is typically taken between 0.15 and 0.35 [23]. To achieve greater thrust, this study selects the ratio of 1/3.

The pareto front of optimization design is shown in the Fig. 6. Finally, the approximate rounding values are h = 84mm, θ =112°, $w_1 = w_2$ = 25mm, and N = 6, with a maximum theoretical obstacle crossing height $(H_1 + H_2)$ of 199.6mm and a maximum forward thrust of 4.83N.

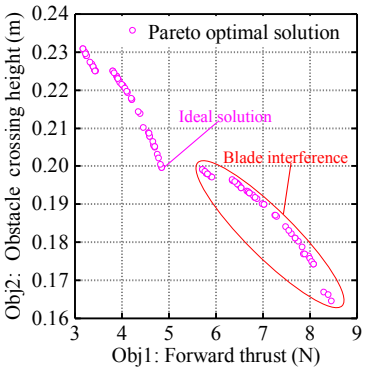

Fig. 6. The pareto front of optimization design.

IV. SIMULATIONS AND DISSCUSSION

The wheel-propeller integrated mechanism can achieve multiple motion modes, exhibiting distinct kinematic and dynamic characteristics under different modes. Based on the multi-objective optimization results, simulations are conducted using the mechanical dynamics simulation software MSC Adams and the fluid dynamics simulation software XFlow. The wheel-propeller integrated mechanisms with different inner and outer hub distances h' are selected for simulation analysis.

A. Single Wheel Propulsion Simulations

When the robot moves on water surface, the wheel-propeller integrated mechanism operates like a screw propeller. When the distance h' between the inner and outer hubs is less than 102mm, the gap between the blades is too narrow, which reduces the propulsion efficiency of the mechanism. Therefore, we selected three sets of inner and outer hub distances h', namely 102mm, 122mm, and 142mm, for single wheel half-submerged propulsion force simulation experiments using XFlow, as shown in Fig.7.

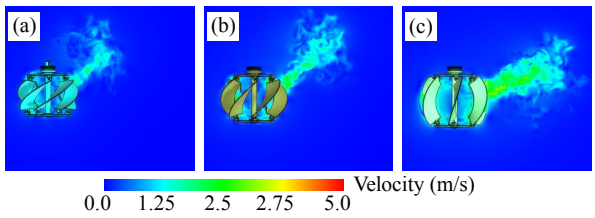

Fig. 7. Propulsion force simulation of different inner and outer hub distance h'. (a) $h' = 102mm$, (b) $h' = 122mm$, (c) $h' = 142mm$.

The spiral direction of the wheel-propeller integrated mechanism have a minimal effect on the propulsion performance. Therefore, a right-handed mechanisms is chosen for the simulation experiments. In the range of 0-240rpm, with intervals of 60rpm, we record the thrust values generated in the X, Y, and Z directions in the base coordinate system for three sets of h' values, as well as the driving torque of a single wheel.

The simulation results, as shown in Fig.8, indicate that the thrust magnitude in the X and Z directions and torque are positively correlated with h'. Usually, the direction of resultant thrust in water is measured by the value of F_X/F_Z, as shown in Table I, there is a difference in F_X/F_Z for different h'. From this, it can be inferred that adjusting the value of h' can change the direction of resultant thrust, thus enabling omnidirectional mobility on water surface.

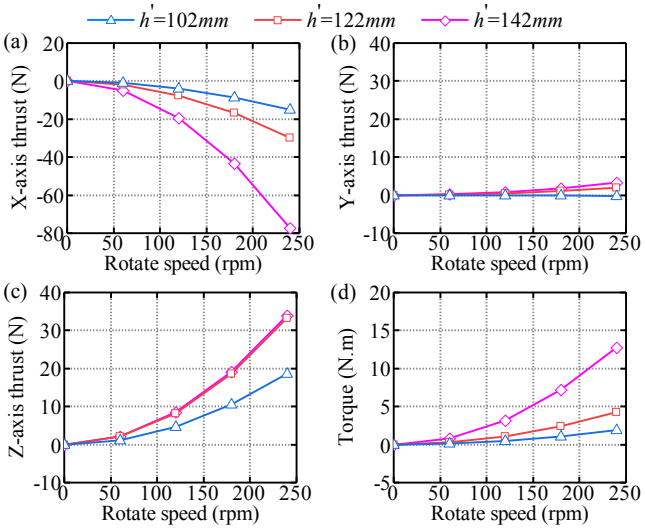

Fig. 8. Thrust and torque magnitude at different rotate speed and h'.

TABLE I
F_X/F_Z AT DIFFERENT h' AND ROTATIONAL SPEEDS.

h'/mm \ n/rpm	60	120	180	240
102	0.841	0.823	0.823	0.812
122	0.917	0.903	0.905	0.897
142	2.288	2.272	2.273	2.268

B. Robot Water Surface Motion Simulations

The overall parameters of the robot are set as follows: the dimensions of the body are 430mm×200mm×120mm (L×W×H), the body weight is approximately 16 kg, and the wheel-propeller integrated mechanism weight is approximately 0.45 kg. The wheel-propeller integrated mechanism is half submerged in water.

The robot is equipped with left-handed wheel-propeller integrated mechanisms on the left front and right rear, but right-handed ones on the right front and left rear. The principle of omnidirectional mobility on water surface is shown in Fig.9. Different motion models can be achieved by using different helix directions and rotation directions.

In the omnidirectional mobility experiment, when the driving torque of the robot's wheel-propeller integrated mechanism is set to 3 N·m, as shown in Fig.10, it can achieve a forward speed of 1.25 m/s, a lateral speed greater than 0.5 m/s, an oblique lateral movement speed of 0.85 m/s and a spot turn speed of 3.5 rad/s at the maximum of h'.

In the oblique lateral movement experiment, the driving torque of the left front and right rear wheel-propeller integrated mechanisms is set to 1 N·m, while the right front

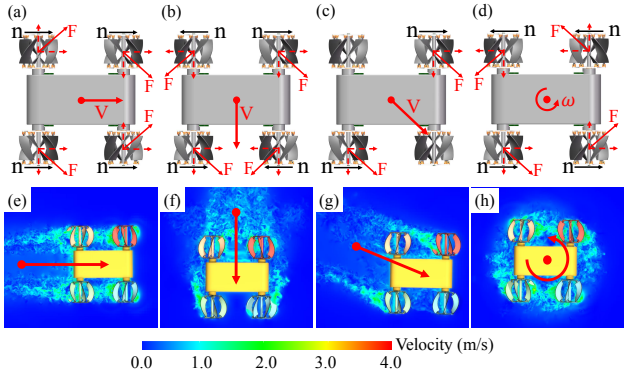

Fig. 9. Water surface motion modes of amphibious robots. (a) Forward motion, (b) Lateral motion, (c) Oblique lateral movement, (d) Spot turn, (e)-(h) The corresponding simulation velocity field.

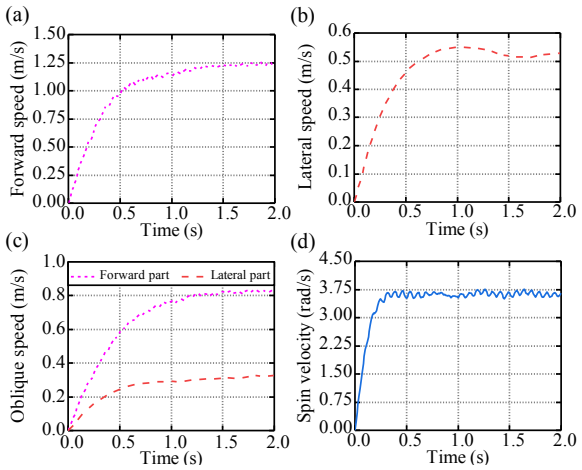

Fig. 10. Motion performance in four motion modes.

and left rear wheel-propeller integrated mechanisms have no driving torque (0 N·m). The motion trajectories of the prototype models with three sets of h' are shown in Fig.11, confirming that varying h' enables the robot to perform oblique lateral movements at different azimuth angles.

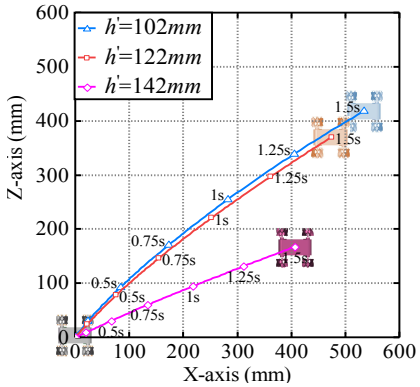

Fig. 11. Oblique lateral movement trajectories of different h'.

C. Land Motion Simulations

In MSC Adams, a virtual prototype model of the wheel-propeller integrated robot is constructed to analyze motion stability and obstacle-crossing performance at different h'. The land motion process is depicted in Fig.12.

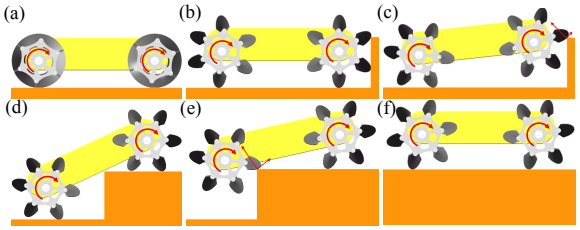

Fig. 12. The land motion process. (a) Flat terrain movement, (b)-(f) Process of crossing the obstacle.

The wheel-propeller integrated mechanism is set to a speed of 60rpm, with a static friction coefficient of 0.7 and a dynamic friction coefficient of 0.5. The total simulation time is limited to 5 seconds, with the initial 1 second dedicated to analyzing motion on flat terrain to assess stability. The subsequent 4 seconds are allocated for obstacle-crossing. During this period, if all the wheel-propeller integrated mechanisms of robot successfully crossed the obstacles, they are considered to possess obstacle-crossing capabilities at that height. obstacle-crossing height and centroid amplitude at different h' is shown in Table II.

TABLE II

OBSTACLE-CROSSING HEIGHT AND CENTROID FLUCTUATION AMPLITUDE AT DIFFERENT h'

h'/mm	42	62	84	102	122	142
Theoretical height/mm	141	147	100	165	183	198
fluctuation amplitude/mm	5.84	8.82	**0.18**	3.42	9.23	15.73
Simulation height/mm	130	147	95	106	149	**184**

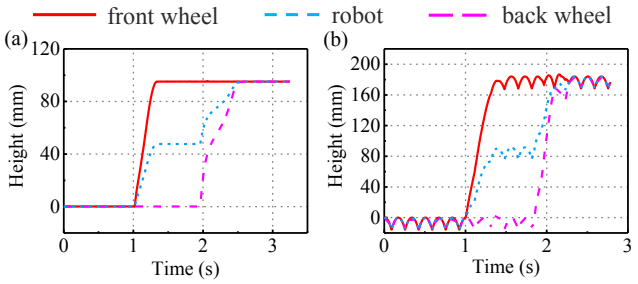

Fig. 13. Obstacle-crossing performance under different h'. (a) $h' = 84$, (b) $h' = 142$.

From Table II, the advantages of the proposed variable wheel-propeller integrated mechanism are evident. When h' is 84mm, the external profile is a complete circle, with a centroid fluctuation amplitude of 0.18mm, enabling rapid movement on flat terrain while minimizing impact vibrations. At h' = 142mm, it achieves the maximum obstacle-crossing height. At a speed of 60rpm, it can cross obstacles as high

as 184mm, making it suitable for navigating unstructured obstacle terrains. The variation in the centroid height for these h' in the simulation is shown in Fig. 13. Additionally, when h' is 42mm, the external profile is serrated, as shown in Fig.1 (a), suitable for soft terrain.

V. CONCLUSIONS

This paper proposes a novel variable wheel-propeller integrated mechanism for amphibious robots. It is characterized by its ability to alter the underwater thrust direction and external profile shape by varying the blade pitch angle. To achieve sufficient motion modes, a comprehensive analysis of the structural parameters' impact on underwater thrust and obstacle-crossing performance is conducted, and optimized design parameters are provided. Ultimately, the optimized wheel-propeller integrated mechanism is integrated into a simulated amphibious robot. Through simulation verification, the wheel-propeller integrated mechanism enables the amphibious robot to achieve multiple motion modes, particularly omnidirectional mobility on the water surface, and exhibits strong adaptability to terrestrial terrains. In future studies, we will conduct more experiments to verify the conclusions in this paper.

REFERENCES

[1] X.-j. Bai, J.-z. Shang, Z.-r. Luo, T. Jiang, and Q. Yin, "Development of amphibious biomimetic robots," *Journal of Zhejiang University-SCIENCE A*, vol. 23, no. 3, pp. 157–187, 2022.

[2] Z. Yan, M. Li, Z. Du, X. Yang, Y. Luo, X. Chen, and B. Han, "Study on a tracked amphibious robot bionic fairing for drag reduction," *Ocean Engineering*, vol. 267, p. 113223, 2023.

[3] J. Yu, R. Ding, Q. Yang, M. Tan, W. Wang, and J. Zhang, "On a bio-inspired amphibious robot capable of multimodal motion," *IEEE/ASME Transactions On Mechatronics*, vol. 17, no. 5, pp. 847–856, 2011.

[4] A. Crespi, K. Karakasiliotis, A. Guignard, and A. J. Ijspeert, "Salamandra robotica ii: an amphibious robot to study salamander-like swimming and walking gaits," *IEEE Transactions on Robotics*, vol. 29, no. 2, pp. 308–320, 2013.

[5] G. Wang, K. Liu, X. Ma, X. Chen, S. Hu, Q. Tang, Z. Liu, M. Ding, and S. Han, "Optimal design and implementation of an amphibious bionic legged robot," *Ocean Engineering*, vol. 272, p. 113823, 2023.

[6] L. Bai, G. Dou, W. Duan, Y. Sun, J. Zheng, and X. Chen, "Amphibious robot with a novel composite propulsion mechanism," in *2021 6th IEEE International Conference on Advanced Robotics and Mechatronics (ICARM)*. IEEE, 2021, pp. 442–447.

[7] P. Burzynski, A. Simha, Ü. Kotta, E. Pawluszewicz, and S. Sastry, "Flhex: a flapped-paddle hexapod for all-terrain amphibious locomotion," *Bulletin of the Polish Academy of Sciences: Technical Sciences*, pp. e139 007–e139 007, 2021.

[8] K. Carpenter, A. Thoesen, D. Mick, J. Martia, M. Cable, K. Mitchell, S. Hovsepian, J. Jasper, N. Georgiev, R. Thakker *et al.*, "Exobiology extant life surveyor (eels)," in *Earth and Space 2021*, 2021, pp. 328–338.

[9] D. A. Schreiber, F. Richter, A. Bilan, P. V. Gavrilov, H. M. Lam, C. H. Price, K. C. Carpenter, and M. C. Yip, "Arcsnake: An archimedes' screw-propelled, reconfigurable serpentine robot for complex environments," in *2020 IEEE International Conference on Robotics and Automation (ICRA)*. IEEE, 2020, pp. 7029–7034.

[10] B. Han, X. Luo, X. Wang, and X. Chen, "Mechanism design and gait experiment of an amphibian robotic turtle," *Advanced Robotics*, vol. 25, no. 16, pp. 2083–2097, 2011.

[11] M. Xia, H. Wang, Q. Yin, J. Shang, Z. Luo, and Q. Zhu, "Design and mechanics of a composite wave-driven soft robotic fin for biomimetic amphibious robot," *Journal of Bionic Engineering*, vol. 20, no. 3, pp. 934–952, 2023.

[12] Z. Chen, Q. Hu, Y. Chen, C. Wei, and S. Yin, "Water surface stability prediction of amphibious bio-inspired undulatory fin robot," in *2021 IEEE/RSJ International Conference on Intelligent Robots and Systems (IROS)*. IEEE, 2021, pp. 7365–7371.

[13] Y. Sun, S. Ma, and X. Luo, "Design of an eccentric paddle locomotion mechanism for amphibious robots," in *2010 IEEE International Conference on Robotics and Biomimetics*. IEEE, 2010, pp. 1098–1103.

[14] H. Pu, C. Liu, Y. Sun, Y. Yang, J. Zou, N. Liu, S. Xie, Y. Peng, and J. Luo, "Optimized non-reciprocating legged gait for an eccentric paddle mechanism," *Robotics and Autonomous Systems*, vol. 103, pp. 83–92, 2018.

[15] Y. Shen, H. Pu, and S. Ma, "Realizing efficient front crawl stroke with a wheel-paddle-integrated mechanism: inspired by human competitive swimming," *IEEE Journal of Oceanic Engineering*, vol. 45, no. 3, pp. 831–839, 2019.

[16] L. Bai, X. Li, Y. Sun, J. Zheng, and X. Chen, "A wheel-legged mobile robot with adjustable body length for rescue and search," in *2021 6th IEEE International Conference on Advanced Robotics and Mechatronics (ICARM)*. IEEE, 2021, pp. 340–345.

[17] J. H. M. Claveria, V. L. R. Esquillo, S. R. M. Regalado, A. J. S. Rodriguez, J. A. T. Chua, J. A. Gonzaga, and L. A. G. Lim, "Wheelbert: A remotely operated ground vehicle for multi-terrain environments," in *2022 IEEE 14th International Conference on Humanoid, Nanotechnology, Information Technology, Communication and Control, Environment, and Management (HNICEM)*. IEEE, 2022, pp. 1–6.

[18] Z. Huang, Y. Yang, P. Lu, and H. Duan, "Motion function transformation and control of amphibious robot based on 4d printing," *JOURNAL OF MECHANICAL ENGINEERING*, vol. 56, no. 15, pp. 39–45, 2020.

[19] Z. Y. Wu, J. Qi, and S. Zhang, "Design of a wheel-propeller integrated amphibious robot and hydrodynamic analysis," *Applied Mechanics and Materials*, vol. 421, pp. 50–55, 2013.

[20] J. Yu, Y. Tang, X. Zhang, and C. Liu, "Design of a wheel-propeller-leg integrated amphibious robot," in *2010 11th International Conference on Control Automation Robotics & Vision*. IEEE, 2010, pp. 1815–1819.

[21] M. Sfakiotakis and D. P. Tsakiris, "A simulation environment for undulatory locomotion," in *Proc. of the International Conference on Applied Simulation and Modelling*, 2004, pp. 28–30.

[22] R. Li, Q. Xiao, Y. Liu, J. Hu, L. Li, G. Li, H. Liu, K. Hu, and L. Wen, "A multi-body dynamics based numerical modelling tool for solving aquatic biomimetic problems," *Bioinspiration & biomimetics*, vol. 13, no. 5, p. 056001, 2018.

[23] F. S. Zha, Z. S. Bing, J. Wang, P. F. Wang, M. T. Li, W. Guo, L. Cheng, and Y. Xia, "Developing of a wheel-paddle integrated propeller for amphibious robot based on moving webbed paddle wheels," *Applied Mechanics and Materials*, vol. 701, pp. 689–696, 2015.